Chemical Engineering Journal 472 (2023) 144924

Contents lists available at ScienceDirect

Chemical Engineering Journal

journal homepage: www.elsevier.com/locate/cej

Revealing dynamic structural evolution of V and P co-doping-induced Co defects as large-current water oxidation catalyst

Lixia Wang [a], Jia Huang [a], Zhiyang Huang [a], Huatong Li [a], Tayirjan Taylor Isimjan [b], Xiulin Yang [a,*]

[a] Guangxi Key Laboratory of Low Carbon Energy Materials, School of Chemistry and Pharmaceutical Sciences, Guangxi Normal University, Guilin 541004, China
[b] Saudi Arabia Basic Industries Corporation (SABIC) at King Abdullah University of Science and Technology (KAUST), Thuwal 23955-6900, Saudi Arabia

ARTICLE INFO

Keywords:
V/P codoped CoS_2
Defect engineering
Surface reconstruction
Water splitting
DFT calculation

ABSTRACT

Metallic defects can improve catalysts' intrinsic activity by regulating its electronic structure and enhancing conductivity. However, the impact of these defects on the kinetics of the oxygen evolution reaction (OER) has not been extensively studied. Here, a V/P codoped nanoflower-like CoS_2 catalyst with rich Co defects on carbon cloth (V,P-CoS_2/CC) is fabricated by feasible directional construction. The V,P-CoS_2/CC validates extraordinary OER performance with overpotentials of 227/300 mV at 10/100 mA cm^{-2} and robust long-term stability. The enhanced single-electron spin resonance signal and higher lifetime strength indicate an increased number of surface Co defects induced by V/P codoping. Density functional theory (DFT) calculations verify that Co defects induced by V/P codoping of the surface reconstituted V-CoOOH/CoS_2 catalyst can optimize the adsorption/desorption energy of oxygen-containing intermediates to accelerate OER process. Besides, the nanoflower-like morphology with large electrochemical active surface area and good hydrophilicity facilitates electrolyte diffusion/gas emission, thereby synergistically elevating OER performance.

1. Introduction

Due to the growing demand for renewable hydrogen energy, water electrolyzers are set to play a vital role in future sustainable hydrogen production systems, owing to their high energy density, zero emissions, and high hydrogen purity [1,2]. The anodic oxygen evolution reaction (OER), which is a pivotal half-reaction in water electrolysis, suffers from slow kinetics, high overpotentials, and low energy efficiency owing to the complex four-electron process ($4OH^- \rightarrow O_2 + 2H_2O + 4e^-$) [3,4]. Therefore, water electrolysis relies on highly active and stable electrocatalysts [5]. Noble metal-based materials such as RuO_2 and IrO_2 have been identified as the most advanced OER catalysts [6,7]. However, their scarcity and high price limit their large-scale commercial application. Consequently, researchers have been exploring inexpensive and efficient non-noble metal catalysts.

Transition metal compounds (TMCs) have been extensively studied as a promising candidate for water splitting due to their environmental benignity, low cost, and high theoretical activity [8,9]. A range of strategies has been reported to enhance the performance of TMCs, such as morphology engineering, construction of heterogeneous interfaces, and doping with anions or cations [10–12]. Among these, doping heteroatoms with different atomic radios and electronegativity is emerging as an effective strategy to modify electronic properties and other chemical activities [13,14]. Cation-doping, particularly the introduction of electron-rich metal heteroatoms, has become one of the most promising ways to design the electronic structure of electrocatalysts and enhance their catalytic performance. This is because they can disrupt the continuity of the local chemical field, alter the charge balance, and thus tune the electronic structure of the interface [15,16]. The V-doping is a well-established approach to improve catalyst performances [17]. Nevertheless, the catalyst community is rarely concerned about the toxicity of vanadium since there is little evidence that vanadium or vanadium compounds are reproductive toxins or teratogens (The Risk Assessment Information System (ornl.gov). For example, Rao et al. introduced the V into low-spin Co_3O_4 (e_g^0) to optimize e_g occupancy ($\approx$ 1.010), ultimately increasing OER activity by about 10% [18]. While anion-doping, especially non-metal heteroatom with high valence, can not only draw into vacancies but also elevate the properties of the inert basal plane to increase the conductivity [19,20]. Zhang et al. synthesized a kind of P-doped Ni-Mo alloy aerogel, which significantly reduced

* Corresponding author.
E-mail address: xlyang@gxnu.edu.cn (X. Yang).

https://doi.org/10.1016/j.cej.2023.144924
Received 11 May 2023; Received in revised form 21 June 2023; Accepted 18 July 2023
Available online 20 July 2023

the electron transfer resistance from 59.5 Ω to 18.4 Ω and showed an ultra-low overpotential of 235 mV at a current of 10 mA cm^{-2} [21]. Aside from single-cation or anion doping, anion/cation co-doping has demonstrated promising improvements in catalyst performance. Li et al. reported highly active and durable OER catalyst by synergistic anionic and cationic co-doping [22]. Additionally, metal defects located at the top of the catalyst can effectively regulate the electronic structure of adjacent atoms, lowering the energy barrier for the reaction intermediate and accelerating the adsorption and dissociation of target molecules, thus enhancing catalytic performance [23]. Three-dimensional (3D) nanoflower structures have been shown to facilitate charge and mass transfer, further improving catalytic performance [24,25]. Furthermore, synthesizing self-supported electrocatalysts on conductive substrates such as carbon cloth or nickel foam can form a strong bond between the active layer and the conductive substrate, thereby improving electronic conductivity through a unique synergistic effect, which facilitates mass transfer at the electrode/electrolyte interface and enhances the durability of the electrocatalyst [26]. The main goal of this study is to combine all these aspects into one catalyst for improved OER performance.

In this work, we propose co-doping of transition metal and anion in a single system to induce the formation of Co defects in CoS_2. The resulting V,P-CoS_2 was grown on a flexible carbon cloth substrate using hydrothermal, sulfidation, and subsequent phosphating treatment, resulting in an efficient catalyst for OER. The V,P-CoS_2/CC electrocatalyst demonstrated impressive OER activity and stability, achieving overpotentials of 227 mV and 300 mV at currents of 10 mA cm^{-2} and 100 mA cm^{-2}, respectively. Moreover, the V,P-CoS_2/CC $^{(+)}$||Pt/C/CC $^{(-)}$ electrolyzer demonstrated robust long-term durability at 10 mA cm^{-2} for 100 h. Through a series of characterizations, we captured dynamic surface reconstruction of V,P-CoS_2/CC, and confirmed that the reconstructed V-CoOOH/CoS_2 was the real active component. DFT studies confirm that the reconfigured V-CoOOH/CoS_2 achieved optimal electronic states and near-ideal binding energies, thereby further improving the OER performance.

2. Experimental procedures

2.1. Materials

All reagents are analytical grade and were used without further purification. Cobalt nitrate hexahydrate ($Co(NO_3)_3{\cdot}6H_2O$) and ruthenium trichloride ($RuCl_3$) were obtained from Shanghai Aladdin Biochemical Technology Co., Ltd. Vanadium chloride (VCl_3), sulfur powder (S), urea ($CO(NH_2)_2$, ≥99.0%), ammonium fluoride (NH_4F, ≥96.0%), sodium hypophosphite monohydrate ($NaH_2PO_2{\cdot}H_2O$, 99%), ethanol absolute (C_2H_5OH, ≥99.7%), Nafion (5% solution), and potassium hydroxide (KOH) were purchased from Guangxi Zoey Biotechnology Co., Ltd. Commercial Pt/C (20 wt% for platinum) was purchased from Alfa Aesar. Sulphuric acid (H_2SO_4, 95.0 ~ 98.0%) was purchased from Xilong Chemical Co., Ltd. The carbon cloth (CC) was obtained from Suzhou Sinero Technology Co., Ltd, and as substrate was used in the experiments (3 cm × 1.5 cm).

2.2. Synthesis of Co-V species on carbon cloth

The CC was ultrasonically washed with 0.5 M H_2SO_4, deionized water and ethanol for 15 min to remove impurities, respectively. 1 mmol ($Co(NO_3)_3{\cdot}6H_2O$), 0.2 mmol VCl_3, 5 mmol urea and 6 mmol NH_4F were dissolved in 25 mL deionized water and 5 mL ethanol to obtain a clear solution. Then the resulting solution was transferred into a 50 mL Teflon-line stainless steel autoclave. The pretreated CC (3 cm × 1.5 cm) was placed obliquely in the autoclave and performed at 120 °C for 12 h. After cooling to room temperature naturally, the obtained product was washed with deionized water several times and dried at room temperature for further use.

2.3. Synthesis of V-CoS_2/CC

The catalyst of V-CoS_2/CC was prepared by coating 0.5 g of sulfur powder on two pieces of Co-V species surface (1 cm × 1.5 cm) and heating (5 °C min^{-1}) to a specific temperature (350, 450 or 550 °C) for 2 h in N_2 atmosphere. Afterwards, the resultant products were rinsed with deionized water and dried at room temperature.

2.4. Synthesis of synthesis of V,P-CoS_2/CC

To convert the V-CoS_2/CC to V,P-CoS_2/CC, two pieces of V-CoS_2/CC (1 cm × 1.5 cm) and 0.5 g of $NaH_2PO_2{\cdot}H_2O$ were placed downstream and upstream of a tube furnace, respectively. Subsequently, the tube furnace was heated slowly to 300 °C (3 °C/min) under N_2 flow for 2 h. Afterwards, the resultant products were rinsed with deionized water and dried at room temperature. The prepared sample was named V,P-CoS_2/CC (from XRD data). The total V,P-CoS_2/CC loading was ~ 5.05 mg cm^{-2}.

In contrast, the synthesis process of V-CoS_2/CC, P-CoS_2/CC and CoS_2/CC were similar to that of V,P-CoS_2/CC, except that P or V sources are not included, respectively.

2.5. Synthesis of RuO_2/NF

The RuO_2 powder was prepared by calcining $RuCl_3$ in the air at 400 °C. Subsequently, the homogeneous catalyst ink was obtained by mixing 2 mg RuO_2/NF with 400 μL of water/ethanol (V/V = 1:1) and 5 μL 5% Nafion as a binder. Then, the mixture was drop-casted onto the CC surface (1 cm × 1.5 cm) and dried in the air.

3. Results and discussion

3.1. Structural and morphological characterizations

V,P-CoS_2/CC was fabricated by a three-step synthesis strategy, as illustrated in Fig. 1a. Firstly, V-Co species/CC nanoflower (Fig. S2a) were uniformly grown on CC through hydrothermal treatment. Subsequently, the V-Co species/CC covered with S powder was annealed at 450 °C (350, 550 °C) to form V doped CoS_2/CC (V-CoS_2/CC). Finally, V, P-CoS_2/CC was obtained by subsequent phosphorylation process. V-CoS_2/CC, P-CoS_2/CC and CoS_2/CC were synthesized by a similar method but without V or P doping. They all showed the morphology of nanoflower in Fig. S2(b-d). The phase chemical composition of the catalysts was characterized by X-ray diffraction (XRD). The XRD patterns of V,P-CoS_2/CC-350, V,P-CoS_2/CC-450, and V,P-CoS_2/CC-550 can be well indexed to CoS_2 (JCPDS: 19–0362) in Fig. 1b [27]. As displayed in Fig. 1c, the XRD patterns of all controls were attributed to CoS_2 except for the broad peak at 26.1°, which corresponds to the amorphous carbon of the carbon cloth support [28]. Notably, the XRD patterns of V,P-CoS_2/CC, V-CoS_2/CC and P-CoS_2/CC showed a slight peak shift compared with that of CoS_2/CC, indicating that the V and P are successfully doped into CoS_2 (Fig. 1d) [29].

The morphology of catalysts was investigated by scanning electron microscopy (SEM) and transmission electron microscopy (TEM), respectively. The SEM images of V,P-CoS_2/CC-350 and V,P-CoS_2/CC-550 show that all the catalysts are agglomerated at both temperature (Fig. S3). According to Fig. 2a, V,P-CoS_2/CC maintained the nanoflower's original morphology, except the petals' surface became thinner and more transparent. As illustrated in Fig. 2c, the TEM image further confirmed the nanoflower-like morphology. In Fig. 2b, high resolution TEM (HR-TEM) images show that the different interplanar spacing of V, P-CoS_2/CC is 0.269 and 0.325 nm, corresponding to the (200) and (111) of CoS_2, respectively. Even more, the selective area electron diffraction (SAED) pattern (Fig. 2d) confirmed that the diffraction ring could be indexed to the (321), (311) and (200) planes of CoS_2, which is consistent with the XRD results. Energy dispersive X-ray spectroscopy

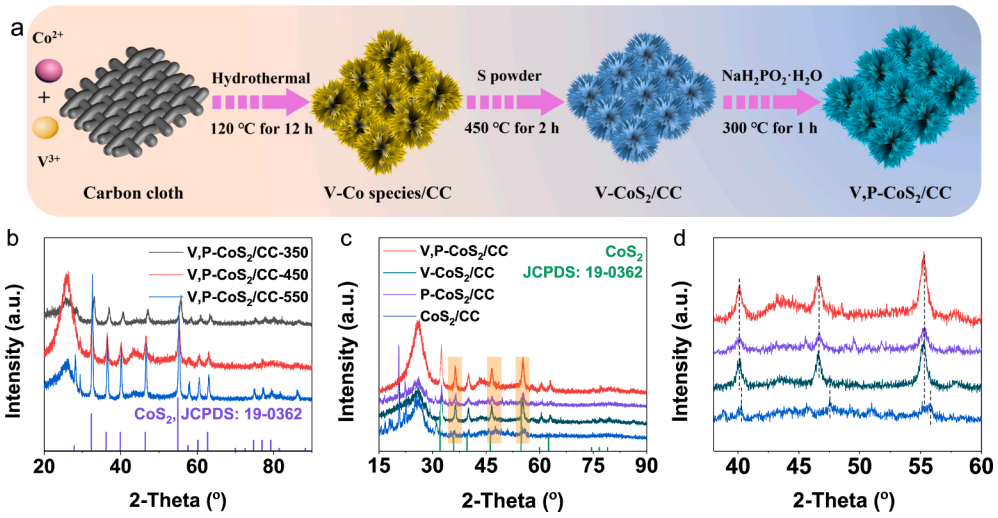

Fig. 1. (a) Schematic illustration for the construction of V,P-CoS_2/CC nanoflower. (b) XRD patterns of V,P-CoS_2/CC at different temperatures (350, 450 and 550 ℃). (c-d) XRD patterns of V,P-CoS_2/CC, P-CoS_2/CC, V-CoS_2/CC and CoS_2/CC.

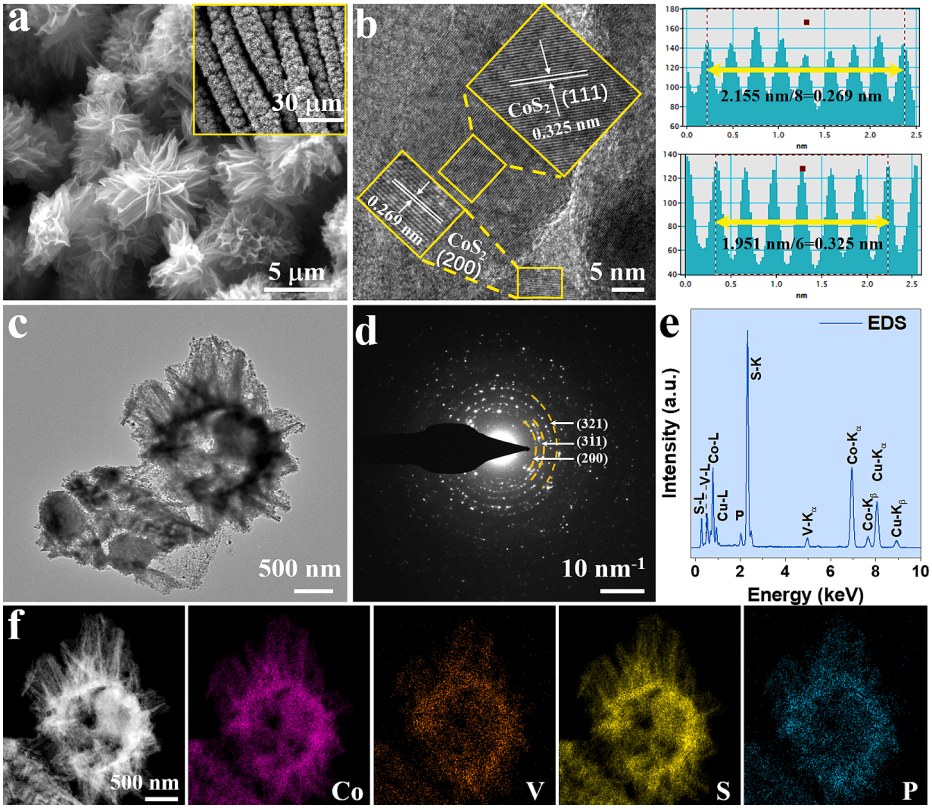

Fig. 2. (a) SEM image, (b) HR-TEM image, (c) TEM image, (d) SAED image, (e) EDS spectrum profile, (f) HAADF-STEM image and corresponding element mappings of V,P-CoS_2/CC.

(EDS) further proved the coexistence of Co, V, S, and P elements with low loading of V and P (Fig. 2e). In addition, the high-angle circular dark-field scanning TEM (HAADF-STEM) image and corresponding elemental mappings revealed the uniform distribution of Co, V, S and P throughout V,P-CoS_2/C (Fig. 2f). Furthermore, actual content of metal elements in the prepared catalysts are detected by inductively coupled plasma mass spectrometry (ICP-MS). The concentrations of Co and V in V,P-CoS_2/CC were 33.25 wt% and 4.72 wt%, respectively, and the Co/V molar ratio was 6.09/1 (Table S2 and S3). The above results confirm that V and P are uniformly incorporated into CoS_2 rather than forming new phases.

Electron paramagnetic resonance (EPR) spectra was conducted to verify the existence of Co defects in the synthesized samples, which can provide valuable information about unpaired electrons [30]. As shown in Fig. 3a, V,P -CoS_2/CC displayed enhanced EPR intensity relative to P-CoS_2/CC, V-CoS_2/CC and original CoS_2/CC, demonstrating the construction of V,P co-doping is beneficial to induce the increase of Co defects in CoS_2. Additionally, positron annihilation lifetime spectroscopy (PALS) is applied to study cation defects' type and relative concentration [31]. The positron lifetime spectrum and the lifetime

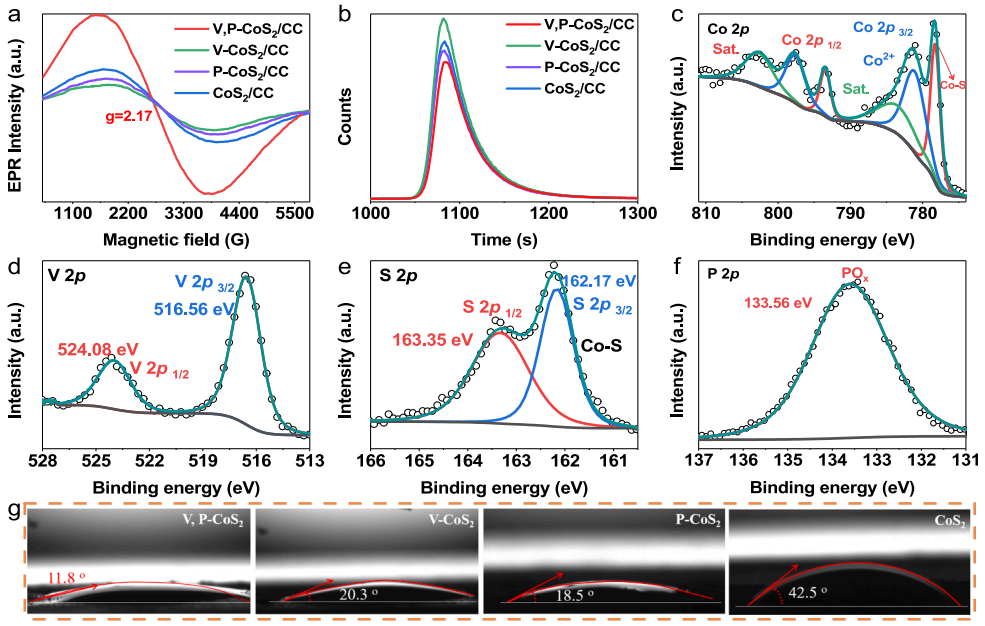

Fig. 3. (a) The EPR spectra, and (b) positron annihilation lifetime spectra of the different catalysts. High-resolution XPS spectra of (c) Co 2*p*, (d) V 2*p*, (e) S 2*p*, and (f) P 2*p* in V,P-CoS_2/CC. (g) Contact angle measurement of the different catalysts.

components of all samples (τ_1, τ_2 and corresponding intensities I_1 and I_2) are shown in Fig. 3b and Table S1, respectively. Among them, τ_1 could be attributed to bulk lifetime and τ_2 should be assigned to positrons annihilation in larger size defects [32]. Since larger defects possess a lower average electron density than minor defects, leading to a lower annihilation rate and increasing the positron lifetime [33]. As a consequence, the τ_2 values of all samples are much larger than the τ_1 values. As a result, V,P-CoS_2/CC exhibits a higher lifetime τ_2 intensity than the other comparative samples, demonstrating the presence of Co defects [33]. The formation of numerous Co defects in V,P-CoS_2/CC facilitates the rapid transfer of ions and simultaneously tune the electronic structure of the electrocatalyst, hence exhibiting excellent surface reaction kinetics [34].

X-ray photoelectron spectroscopy (XPS) analysis revealed V,P-CoS_2/CC valence and elemental composition. As depicted in Fig. S4a, the full survey spectrum of V,P-CoS_2/CC demonstrates the existence of Co, V, S and P elements, which is consistent with the TEM results. The high-resolution C 1 *s* spectrum is deconvoluted into four peaks, including C = O (284.0 eV), C–C (284.8 eV), C–O (286.0 eV) and C = O (288.0 eV). This work uses the binding energies based on C 1 *s* as the standard for correction (Fig. S4b). Depicted as Fig. 3c, the Co 2*p* XPS spectrum of V,P-CoS_2/CC shows two prominent peaks at 778.33 and 793.51 eV, which are assigned to Co-S compounds. The other two peaks located at 781.38 and 797.77 eV are ascribed to the characteristic peaks of Co^{2+} in CoS_2,

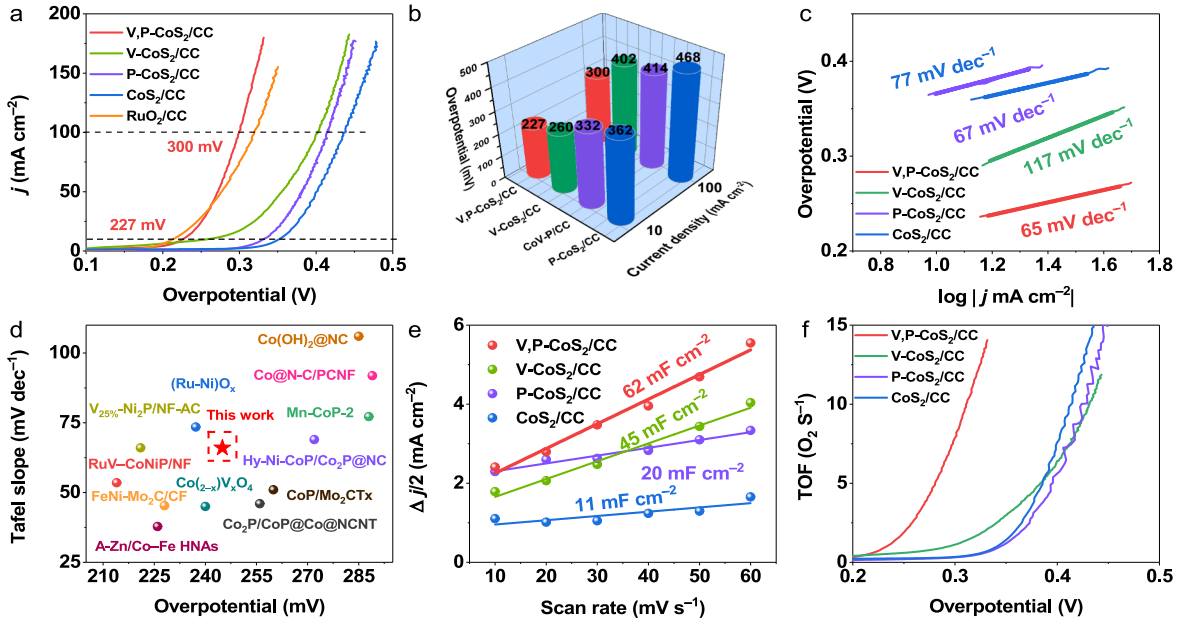

Fig. 4. OER performance of different catalysts and RuO_2/CC in 1.0 M KOH. (a) LSV polarization curves, (b) overpotential comparison at 10 and 100 mA cm^{-2}, (c) corresponding Tafel slopes, (d) comparison with the overpotentials of recently reported catalysts for OER activity at 10 mA cm^{-2}, (e) double layer capacitance (C_{dl}), and (f) turnover frequency (TOF) value.

and at 784.34 and 802.83 eV are satellite peaks, respectively [35]. Fig. 3d displays the high-resolution V 2*p* XPS spectrum. The two peaks at 516.56 and 524.08 eV can be attributed to the V $2p_{3/2}$ and $2p_{1/2}$ states [36]. The core-level spectrum of S 2*p* (Fig. 3e) exhibits two peaks at 162.28 and 163.46 eV of S $2p_{3/2}$ and S $2p_{1/2}$ belong to Co-S in the hydride [37]. And Fig. 3f reveals the P 2*p* region of V,P-CoS_2/CC. The binding energy at 133.56 eV are assigned to PO_x, demonstrating the successful doping of P [38]. The above results confirmed the successful preparation of V,P-CoS_2. Furthermore, the wettability of the electrocatalyst is a vital parameter that influences the electrochemical performance. The hydrophilicity of the electrocatalyst is beneficial for promoting OER activity due to its solid–liquid interfacial activity [39]. Impressively, the contact angle on V,P-CoS_2/CC is 11.8° (Fig. 3g), which is smaller than that P-CoS_2/CC (18.5°), V-CoS_2/CC (20.3°) and CoS_2/CC (42.5°), confirming the better hydrophilicity of V,P-CoS_2/CC, which is conducive to the adsorption of reactant H_2O and promotes the oxygen evolution process [40].

3.2. Electrocatalytic performance

The electrocatalytic oxygen evolution activity of the prepared catalysts was investigated using linear sweep voltammetry (LSV) in 1.0 M KOH solution. Since the sulfidation temperature significantly influences the catalytic performance, samples obtained by sulfidation at various temperatures were initially evaluated for OER activity, and the results indicate the optimum temperature was 450 °C (Fig. S5). LSV curves (Fig. 4a) show that the V,P-CoS_2/CC exhibits superior OER activity, requiring only a much lower overpotential of 227 mV at 10 mA cm^{-2} than those of V-CoS_2/CC (260 mV), P-CoS_2/CC (332 mV), CoS_2/CC (362 mV). Although, the overpotential of V,P-CoS_2/CC is slightly higher than that of RuO_2 at 10 mA cm^{-2}, V,P-CoS_2/CC outperforms RuO_2 when the current density exceeds 40 mA cm^{-2}, indicating superior industrial application potential under high current density compares to the RuO_2 catalyst. Meanwhile, the overpotentials with current densities of 10 and 100 mA cm^{-2} was selected as the comparison parameters. The corresponding results are displayed in Fig. 4b. The optimized V,P-CoS_2/CC exhibited an enhanced OER activity compared to the individual V-CoS_2/CC, P-CoS_2/CC and CoS_2/CC, highlighting the essential synergistic effect of V and P co-doping. The Tafel slope of the catalyst was obtained by fitting the polarization curve in the kinetic range (Fig. 4c). As expected, the Tafel slope of the V,P-CoS_2/CC was measured to be 66 mV dec^{-1}, lower than the V-CoS_2/CC (117 mV dec^{-1}), P-CoS_2/CC (67 mV dec^{-1}) and CoS_2/CC (77 mV dec^{-1}), implying the enhanced reaction kinetics of V,P-CoS_2/CC [41]. V,P-CoS_2/CC also exhibits reasonably good OER activity among the recently reported heteroatom-doped CoS_2 and other transition metal OER catalysts (Fig. 4d and Tables S4-5). The electrochemically active surface area (ECSA) of the different catalysts were estimated based on the double layer capacitance (C_{dl}) to investigate the origin of the increased OER activity. The C_{dl} was also calculated from the cyclic voltammetry (CV) curve at different scan rates (Figs. S6-7) in the non-Faradaic range. The V,P-CoS_2/CC exhibited the C_{dl} value of 62 mF cm^{-2}, higher than V-CoS_2/CC (45 mF cm^{-2}), P-CoS_2/CC (20 mF cm^{-2}) and CoS_2/CC (11mF cm^{-2}), respectively (Fig. 4e). The ECSA value of V, P-CoS_2/CC is 1033.3 cm^{-2} (normalized to per cm^2 of electrode area), which is 1.4-, 3.1-, and 5.6-fold higher than V-CoS_2/CC, P-CoS_2/CC and CoS_2/CC, manifesting that V and P co-doping effectively increased the ECSA of CoS_2 (Fig. S8). Furthermore, the turnover frequency (TOF) is considered one of the most reasonable parameters for assessing the inherent activity of the catalysts, which represents the amount of O_2 molecules released per second per active site [42]. V,P-CoS_2/CC showed a higher TOF value than other samples (Fig. 4f), indicating that V and P co-doping significantly enhanced the intrinsic activity of CoS_2 for OER. Based on the equivalent circuit model, the electrochemical impedance spectroscopy (EIS) of V,P-CoS_2/CC (Fig. S9a) illustrated the smallest charge transfer resistance (R_{ct}) values compared to other controls (Fig. S9b), revealing the faster charge transfer kinetics between the V,P-CoS_2/CC and the electrolyte [43]. In addition, the long-term stability of V,P-CoS_2/CC was tested by constant current and cyclic voltammetry methods. The current densities of V,P-CoS_2/CC can be maintained for 100 h without considerable potential increase at a current density of 10 mA cm^{-2} (Fig. S10a). The LSV curve after 1000 CV cycles is consistent with the initial one (Fig. S10b), implying that V,P-CoS_2/CC has exceptional stability.

Considering the superior OER performance of V,P-CoS_2/CC, a two-electrode overall water splitting device was assembled by employing the V,P-CoS_2/CC as anode and 20 wt% Pt/C/CC as cathode, respectively, and schematically presented in Fig. 5a. As expected, the V,P-CoS_2/CC $^{(+)}$||Pt/C/CC $^{(-)}$ acquired a cell voltage of 1.87 V to deliver a current density of 500 mA cm^{-2}, which is lower than that of the RuO_2/CC $^{(+)}$||Pt/C/CC $^{(-)}$ (1.95 V) in Fig. 5b. Importantly, during the electrochemical test, O_2 and H_2 bubbles can be observed on the anode and cathode surfaces during electrochemical testing (inset in Fig. 5b). Encouragingly, the required voltage of the V,P-CoS_2/CC $^{(+)}$||Pt/C/CC $^{(-)}$ to afford the current density of 10 mA cm^{-2} also surpasses the state-of-the-art reported other electrocatalysts for alkaline overall water splitting (Fig. 5c and Table S6). Moreover, the V,P-CoS_2/CC $^{(+)}$||Pt/C/CC $^{(-)}$ revealed robust long-term durability at 10 mA cm^{-2} for 100 h, suggesting the superior stability of the V,P-CoS_2/CC $^{(+)}$||Pt/C/CC $^{(-)}$ device (Fig. 5d).

3.3. Structural evolution analysis and DFT calculation

In situ surface reconfiguration inevitably occurs in the highly oxidative environment of the catalyst in the OER progress [44]. Consequently, further investigation of the reconstructed catalyst's structure is essential. Interestingly, from the SEM image, the catalyst morphology was changed from a thin nanoflower to a rough surface litchi shape after stability testing, which is consistent with the results of the TEM image (Fig. S11a-b). According to the XRD results (Fig. 6a), the peak of CoS_2 (JCPDS: 02–0214) completely disappeared, signifying that V,P-CoS_2 is reconstructed as CoOOH with low crystallinity on the catalyst surface [45]. Moreover, HR-TEM showed relatively few crystal fringes corresponding to the (0 1 2) plane of CoOOH (Fig. S11c), while SAED also confirmed that it somewhat lost the crystallinity after the stability test (Fig. S11d). Compared to the initial EDS and corresponding element mappings, the O content dramatically increased while V, P and S all decreased (Fig. S11e-f). The XPS results (Fig. S12) showed that the

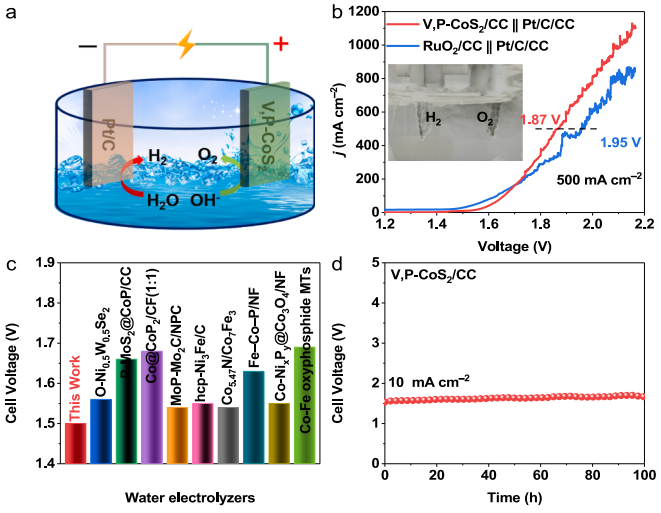

Fig. 5. (a) Schematic diagram of overall water splitting electrolyzer using V,P-CoS_2/CC and Pt/C/CC as anode and cathode, respectively. (b) Comparison of polarization curves of V,P-CoS_2/CC $^{(+)}$||Pt/C/CC $^{(-)}$ and the RuO_2/CC $^{(+)}$||Pt/C/CC $^{(-)}$ at high currents in 1.0 M KOH. (c) Comparing cell voltages with the recently reported electrolyzers at 10 mA cm^{-2} in 1.0 M KOH. (d) Long-term stability test of V,P-CoS_2/CC $^{(+)}$||Pt/C/CC $^{(-)}$ at 10 mA cm^{-2} in 1.0 M KOH.

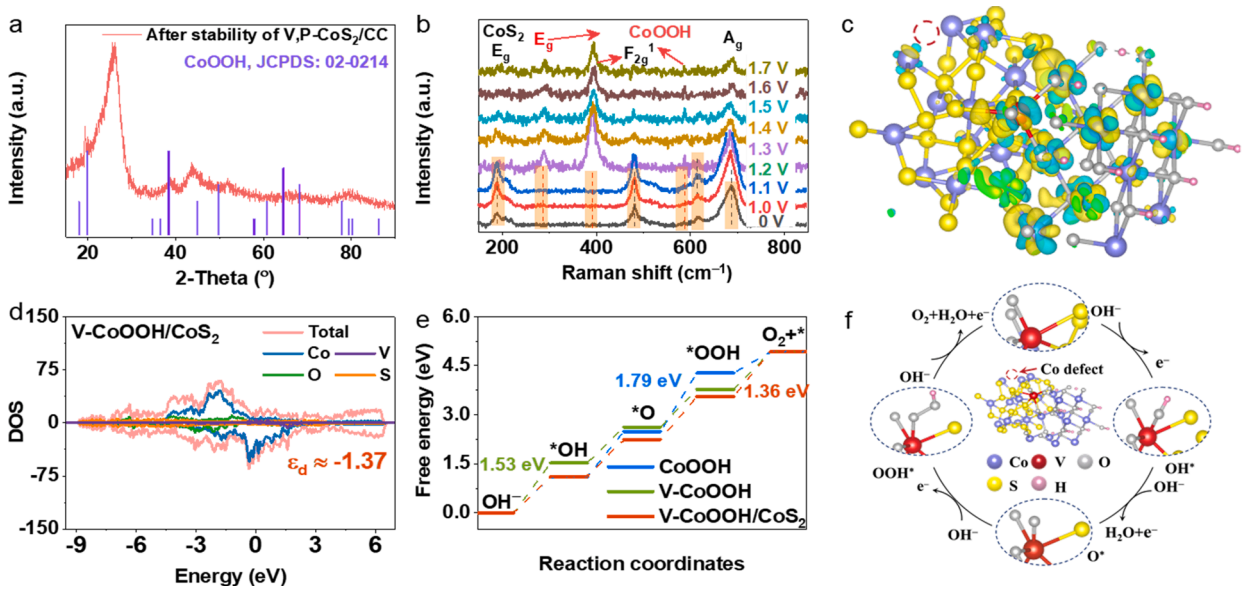

Fig. 6. (a) XRD pattern of V,P-CoS_2/CC after OER stability test. (b) In-situ Raman spectra of V,P-CoS_2/CC catalyst under OER condition. (c) Differential charge density diagram of V-CoOOH/CoS_2, where Co, V, O, H, and S are represented by violet, red, gray, pink and yellow spheres, respectively. (d) Density of states (DOS) of V-CoOOH/CoS_2. (e) Free energy diagrams of the OER processed on different catalysts. (f) OER mechanism illustration of V-CoOOH/CoS_2.

Co-S disappeared for the Co 2p region, and the binding energy located at 779.1 eV was attributed to the Co^{3+} configurations [46]. Furthermore, V 2*p* spectrum displayed a decrease in the peak intensity. The O 1 *s* spectrum appear at 530.0, 530.8 and 531.8 eV assigned to M−O, OH^-, and H_2O_{ads}, respectively, implying that the surface layer of the catalyst was oxidized. As illustrated in S 2*p* spectrum, the intensity of Co-S characteristic peaks decreased, indicating that a significant amount of S leaching occurred, while the peaks at 167.5 and 168.6 eV corresponded to the S-O bond [47]. As for the P 2*p* spectrum, the almost negligible variation may be attributed to the low P content. To further confirm the change of V,P-CoS_2 during OER, in-situ Raman was used to observe structural evolution during the electrochemical test (Fig. 6b). Surprisingly, four characteristic peaks of CoS_2 were observed in three consecutive potentials between OCP and 1.1 V at ~ 192, 482, 619 and 688 cm^{-1} [48]. The peaks of CoS_2 gradually weaken when the potential increased, and the characteristic peaks that well match with CoOOH appeared at 290, 391 and 586 cm^{-1} [49]. These facts indicated the collapse of the V,P-CoS_2 and the in-situ redeposition of CoOOH on the catalyst surface during OER, suggesting that leaching of S species can lead to the transformation of a genuinely active site from V,P-CoS_2 catalyst to V-CoOOH/CoS_2.

Consequently, to further elucidate the role of Co defects and in-situ reconstruction from V,P-CoS_2 to V-CoOOH/CoS_2 heterojunctions (assuming the metal as the active center) on improving catalytic performance for OER in atomic level. Three different theoretical computational models, CoOOH, V-doped CoOOH (V-CoOOH) and V-doped CoOOH/CoS_2 heterostructure with Co defects (V-CoOOH/CoS_2) were constructed based on the (0 1 2) and (3 1 1) lattice planes of CoOOH and CoS_2, as illustrated in Fig. S14. Notably, the charge density differences result in significant charge accumulation at the interface of CoOOH and CoS_2 (Fig. 6c), which can effectively adjust the adsorption energy of the reaction sites to the intermediates and accelerate the OER reaction kinetics [50]. The density of states (DOS) and *d*-band center (ε_d) for CoOOH, V-CoOOH and V-CoOOH/CoS_2 are displayed in Fig. S13 and Fig. 6d. Obviously, the CoOOH, V-CoOOH and V-CoOOH/CoS_2 all manifest different intrinsic metallicity, attesting high conductivity and fast electron transfer, favoring the OER kinetics [10]. The introduction of V in CoOOH shifts ε_d toward the Fermi level. Meanwhile, V-CoOOH/CoS_2 causes ε_d to shift away from the Fermi level, leading to suitable intermediates adsorption/desorption performance during the OER process [51]. Remarkably, the Gibbs free energy diagram of the OER process for the intermediates adsorbed on different samples is depicted in Fig. 6e. Impressively, it shows that when U = 0 V, all reaction steps of the three catalysts undergo an uphill (internal heat) process. For V-CoOOH/CoS_2, the step from *OOH to O_2 presents the smallest energy barrier of 1.36 eV ($|\Delta G_{H^*}|$), indicating that it is the rate-determining step (RDS). However, the RDS for CoOOH is from *O to *OOH ($|\Delta G_{H^*}|$ =1.79 eV), while the RDS for V-CoOOH is the first step from OH^- to *OH ($|\Delta G_{H^*}|$ =1.53 eV). This result implies that the Co defects in V-CoOOH/CoS_2 allow for weak *OOH adsorption, which drives easier release of the generated O_2 from the catalyst surface. Significantly, the energy barrier of V-CoOOH/CoS_2 decreased dramatically compared with CoOOH and V-CoOOH, confirming that V-CoOOH/CoS_2 can optimize the adsorption and desorption properties of the reaction intermediates, significantly reduce the reaction energy barrier, and accelerate the reaction kinetics to improve the OER activity [52]. The corresponding OER mechanism of V-CoOOH/CoS_2, CoOOH and V-CoOOH are showed in Fig. 6f and Figs. S15-16. We proposed a four-step OER mechanism as the following:

$$* + OH^- \rightarrow *OH + e^- \quad (1)$$

$$*OH + OH^- \rightarrow *O + H_2O + e^- \quad (2)$$

$$*O + OH^- \rightarrow *OOH + e^- \quad (3)$$

$$*OOH + OH^- \rightarrow O_2 + H_2O + e^- \quad (4)$$

Foremost, OH^- is oxidized to obtain *OH and loses an electron by attaching it to the V-CoOOH/CoS_2 surface. Then, *OH undergoes proton-coupled electron transfer with OH^- to form *O. Subsequently, another OH^- attacks a proton and deprotonates to form the intermediate *OOH. Eventually, the proton-coupled electron transfer leads to the release of O_2 [53].

4. Conclusions

In summary, a simple hydrothermal and two-step calcination process of preparing a novel V,P-CoS_2/CC with abundant Co defects was reported. The nanoflower-like structure supports the exposure of more reaction sites, ensuring electrolyte accessibility and available bubble release. Significantly, the V,P-CoS_2/CC exhibits enhanced OER catalytic performance with overpotentials of 227/300 mV@10/100 mA cm^{-2} in

1.0 M KOH. The assembled water-splitting electrolyzer requires only 1.87 V to deliver 500 mA cm^{-2} and achieve robust stability over 100 h. DFT calculations confirm that V-CoOOH/CoS_2 interface with Co defects can optimize adsorption/desorption of the intermediates and thus promote the OER reaction kinetics. This work achieves in-situ surface reconstruction and reveals that anion/cation double doping induces metal defects to enhance OER performance.

CRediT authorship contribution statement

Lixia Wang: Investigation, Data curation, Writing - original draft. **Jia Huang:** Investigation. **Zhiyang Huang:** Data curation. **Huatong Li:** Investigation, Methodology. **Tayirjan Taylor Isimjan:** Writing – review & editing. **Xiulin Yang:** Supervision, Writing - review & editing.

Declaration of Competing Interest

The authors declare that they have no known competing financial interests or personal relationships that could have appeared to influence the work reported in this paper.

Data availability

Data will be made available on request.

Acknowledgements

This work has been supported by the National Natural Science Foundation of China (no. 21965005), Natural Science Foundation of Guangxi Province (2018GXNSFAA294077, 2021GXNSFAA076001), Project of High-Level Talents of Guangxi (F-KA18015), Guangxi Technology Base and Talent Subject (GUIKE AD18126001, GUIKE AD20297039), and Innovation Project of Guangxi Graduate Education (YCBZ2023056).

Appendix A. Supplementary data

Supplementary data to this article can be found online at https://doi.org/10.1016/j.cej.2023.144924.

References

[1] T.L.L. Doan, D.C. Nguyen, S. Prabhakaran, D.H. Kim, D.T. Tran, N.H. Kim, J.H. Lee, Single-Atom Co-Decorated MoS_2 Nanosheets Assembled on Metal Nitride Nanorod Arrays as an Efficient Bifunctional Electrocatalyst for pH-Universal Water Splitting, Adv. Funct. Mater. 31 (2021) 2100233, https://doi.org/10.1002/adfm.202100233.

[2] Z. Xu, S. Li, W. Lu, X. Dou, Y. Wu, J. Zeng, Y. Dou, J. Zhang, J. Wei, L. Yu, In-Situ construction of hierarchically porous CoNiP/MP Ni electrocatalyst for overall water splitting, Fuel 348 (2023), 128400, https://doi.org/10.1016/j.fuel.2023.128400.

[3] Z. Liu, C. Zhang, H. Liu, L. Feng, Efficient synergism of $NiSe_2$ nanoparticle/NiO nanosheet for energy-relevant water and urea electrocatalysis, Appl. Catal. B: Environ. 276 (2020), 119165, https://doi.org/10.1016/j.apcatb.2020.119165.

[4] P. Yan, M. Huang, B. Wang, Z. Wan, M. Qian, H. Yan, T.T. Isimjan, J. Tian, X. Yang, Oxygen defect-rich double-layer hierarchical porous Co_3O_4 arrays as high-efficient oxygen evolution catalyst for overall water splitting, J. Energy Chem. 47 (2020) 299–306, https://doi.org/10.1016/j.jechem.2020.02.006.

[5] R. He, M. Li, W. Qiao, L. Feng, Fe doped Mo/Te nanorods with improved stability for oxygen evolution reaction, Chem. Eng. J. 423 (2021), 130168, https://doi.org/10.1016/j.cej.2021.130168.

[6] Q. Peng, Q. He, Y. Hu, T.T. Isimjan, R. Hou, X. Yang, Interface engineering of porous Fe_2P-$WO_{2.92}$ catalyst with oxygen vacancies for highly active and stable large-current oxygen evolution and overall water splitting, J. Energy Chem. 65 (2022) 574–582, https://doi.org/10.1016/j.jechem.2021.06.037.

[7] J. Zhao, Y. Zhang, Y. Xia, B. Zhang, Y. Du, B. Song, H.-L. Wang, S. Li, P. Xu, Strong phosphide-metaphosphate interaction in RuP/$CoNiP_4O_{12}$ for enhanced electrocatalytic water splitting, Appl. Catal. B: Environ. 328 (2023), 122447, https://doi.org/10.1016/j.apcatb.2023.122447.

[8] Y. Ko, J. Park, J. Mo, S. Lee, Y. Song, Y. Ko, H. Lee, Y. Kim, J. Huh, S.W. Lee, J. Cho, Layer-by-Layer Assembly-Based Electrocatalytic Fibril Electrodes Enabling Extremely Low Overpotentials and Stable Operation at 1 A cm^{-2} in Water-Splitting Reaction, Adv. Funct. Mater. 31 (2021) 2102530, https://doi.org/10.1002/adfm.202102530.

[9] W. Xu, W. Zhong, C. Yang, R. Zhao, J. Wu, X. Li, N. Yang, Tailoring interfacial electron redistribution of Ni/Fe_3O_4 electrocatalysts for superior overall water splitting, J. Energy Chem. 73 (2022) 330–338, https://doi.org/10.1016/j.jechem.2022.06.042.

[10] Y. Hu, Z. Luo, M. Guo, J. Dong, P. Yan, C. Hu, T.T. Isimjan, X. Yang, Interface engineering of $Co_2N_{0.67}$/$CoMoO_4$ heterostructure nanosheets as a highly active electrocatalyst for overall water splitting and Zn-H_2O cell, Chem. Eng. J. 435 (2022) 134795, https://doi.org/10.1016/j.cej.2022.134795.

[11] S. Javaid, X. Xu, W. Chen, J. Chen, H.-Y. Hsu, S. Wang, X. Yang, Y. Li, Z. Shao, F. Jones, G. Jia, Ni^{2+}/Co^{2+} doped Au-Fe_7S_8 nanoplatelets with exceptionally high oxygen evolution reaction activity, Nano Energy 89 (2021), 106463, https://doi.org/10.1016/j.nanoen.2021.106463.

[12] L. Li, X. Cao, J. Huo, J. Qu, W. Chen, C. Liu, Y. Zhao, H. Liu, G. Wang, High valence metals engineering strategies of Fe/Co/Ni-based catalysts for boosted OER electrocatalysis, J. Energy Chem. 76 (2023) 195–213, https://doi.org/10.1016/j.jechem.2022.09.022.

[13] J. Zhang, J. Zhang, F. He, Y. Chen, J. Zhu, D. Wang, S. Mu, H.Y. Yang, Defect and Doping Co-Engineered Non-Metal Nanocarbon ORR Electrocatalyst, Nano-Micro Lett. 13 (2021) 65, https://doi.org/10.1007/s40820-020-00579-y.

[14] Y. Zhou, Y. Wang, H. Zhao, J. Su, H. Zhang, Y. Wang, Investigation of anion doping effect to boost overall water splitting, J. Catal. 381 (2020) 84–95, https://doi.org/10.1016/j.jcat.2019.10.026.

[15] X. Chen, Y. Li, H. Xing, S. Fei, L. Ma, R. Tu, A. Huang, W.-C. Cheong, Q. Liu, R. Ge, S. Liu, D. Liu, X. Wei, K. Wu, X. Chen, C. Chen, Combination of Fe(II)-induced oxygen deficiency and metal doping strategy for construction of high efficiency water oxidation electrocatalysts under industrial-scale current density, Chem. Eng. J. 435 (2022), 135048, https://doi.org/10.1016/j.cej.2022.135048.

[16] L. Ma, K. Zhang, S. Wang, L. Gao, Y. Sun, Q. Liu, J. Guo, X. Zhang, Vanadium doping over Ni_3S_2 nanosheet array for improved overall water splitting, Appl. Surf. Sci. 489 (2019) 815–823, https://doi.org/10.1016/j.apsusc.2019.06.044.

[17] P. Zhou, X. Lv, D. Xing, F. Ma, Y. Liu, Z. Wang, P. Wang, Z. Zheng, Y. Dai, B. Huang, High-efficient electrocatalytic overall water splitting over vanadium doped hexagonal $Ni_{0.2}Mo_{0.8}N$, Appl. Catal. B Environ. 263 (2020), 118330, https://doi.org/10.1016/j.apcatb.2019.118330.

[18] Y. Rao, S. Chen, Q. Yue, Y. Kang, Optimizing the Spin States of Mesoporous Co_3O_4 Nanorods through Vanadium Doping for Long-Lasting and Flexible Rechargeable Zn–Air Batteries, ACS Catal. 11 (2021) 8097–8103, https://doi.org/10.1021/acscatal.1c01585.

[19] W. Yao, C. Tian, C. Yang, J. Xu, Y. Meng, I. Manke, N. Chen, Z. Wu, L. Zhan, Y. Wang, R. Chen, P-Doped $NiTe_2$ with Te-Vacancies in Lithium-Sulfur Batteries Prevents Shuttling and Promotes Polysulfide Conversion, Adv. Mater. 34 (2022) 2106370, https://doi.org/10.1002/adma.202106370.

[20] F. Liu, N. Wang, C. Shi, J. Sha, L. Ma, E. Liu, N. Zhao, Phosphorus doping of 3D structural MoS_2 to promote catalytic activity for lithium-sulfur batteries, Chem. Eng. J. 431 (2022), 133923, https://doi.org/10.1016/j.cej.2021.133923.

[21] B. Zhang, F. Yang, X. Liu, N. Wu, S. Che, Y. Li, Phosphorus doped nickel-molybdenum aerogel for efficient overall water splitting, Appl. Catal. B: Environ. 298 (2021), 120494, https://doi.org/10.1016/j.apcatb.2021.120494.

[22] Z. Li, K.-H. Xue, J. Wang, J.-G. Li, X. Ao, H. Sun, X. Song, W. Lei, Y. Cao, C. Wang, Cation and Anion Co-doped Perovskite Nanofibers for Highly Efficient Electrocatalytic Oxygen Evolution, ACS Appl. Mater. Interfaces 12 (2020) 41259–41268, https://doi.org/10.1021/acsami.0c10045.

[23] J. Sun, H. Xue, Y. Zhang, X.-L. Zhang, N. Guo, T. Song, H. Dong, Y. Kong, J. Zhang, Q. Wang, Unraveling the Synergistic Effect of Heteroatomic Substitution and Vacancy Engineering in $CoFe_2O_4$ for Superior Electrocatalysis Performance, Nano Lett. 22 (2022) 3503–3511, https://doi.org/10.1021/acs.nanolett.1c04425.

[24] H. Liao, X. Zhang, S. Niu, P. Tan, K. Chen, Y. Liu, G. Wang, M. Liu, J. Pan, Dynamic dissolution and re-adsorption of molybdate ion in iron incorporated nickel-molybdenum oxyhydroxide for promoting oxygen evolution reaction, Appl. Catal. B: Environ. 307 (2022), 121150, https://doi.org/10.1016/j.apcatb.2022.121150.

[25] J. Liu, L. Zhang, H. Wu, Anion-Doping-Induced Vacancy Engineering of Cobalt Sulfoselenide for Boosting Electromagnetic Wave Absorption, Adv. Funct. Mater. 32 (2022) 2200544, https://doi.org/10.1002/adfm.202200544.

[26] M. Biswal, A. Deshpande, S. Kelkar, S. Ogale, Water Electrolysis with a Conducting Carbon Cloth: Subthreshold Hydrogen Generation and Superthreshold Carbon Quantum Dot Formation, ChemSusChem 7 (2014) 883–889, https://doi.org/10.1002/cssc.201300827.

[27] Y.-Y. Zhang, X. Zhang, Z.-Y. Wu, B.-B. Zhang, Y. Zhang, W.-J. Jiang, Y.-G. Yang, Q.-H. Kong, J.-S. Hu, Fe/P dual doping boosts the activity and durability of CoS_2 polycrystalline nanowires for hydrogen evolution, J. Mater. Chem. A 7 (2019) 5195–5200, https://doi.org/10.1039/C8TA12269E.

[28] Q. Peng, X. Zhuang, L. Wei, L. Shi, T.T. Isimjan, R. Hou, X. Yang, Niobium-Incorporated $CoSe_2$ Nanothorns with Electronic Structural Alterations for Efficient Alkaline Oxygen Evolution Reaction at High Current Density, ChemSusChem 15 (2022), e202200827, https://doi.org/10.1002/cssc.202200827.

[29] W. Peng, A. Deshmukh, N. Chen, Z. Lv, S. Zhao, J. Li, B. Yan, X. Gao, L. Shang, Y. Gong, L. Wu, M. Chen, T. Zhang, H. Gou, Deciphering the Dynamic Structure Evolution of Fe- and Ni-Codoped CoS_2 for Enhanced Water Oxidation, ACS Catal. 12 (2022) 3743–3751, https://doi.org/10.1021/acscatal.2c00328.

[30] Y. Hu, M. Guo, C. Hu, J. Dong, P. Yan, T. Taylor Isimjan, X. Yang, Engineering cobalt nitride nanosheet arrays with rich nitrogen defects as a bifunctional robust oxygen electrocatalyst in rechargeable Zn–air batteries, J. Colloid Interface Sci. 608 (2022) 2066–2074, https://doi.org/10.1016/j.jcis.2021.10.128.

[31] J. Bai, Y. Li, P. Wei, J. Liu, W. Chen, L. Liu, Enhancement of Photocatalytic Activity of Bi_2O_3–BiOI Composite Nanosheets through Vacancy Engineering, Small 15 (2019) 1900020, https://doi.org/10.1002/smll.201900020.
[32] F.A. Selim, Positron annihilation spectroscopy of defects in nuclear and irradiated materials- a review, Mater Charact 174 (2021), 110952, https://doi.org/10.1016/j.matchar.2021.110952.
[33] J. Sun, H. Xue, N. Guo, T. Song, Y.R. Hao, J. Sun, J. Zhang, Q. Wang, Synergetic Metal Defect and Surface Chemical Reconstruction into $NiCo_2S_4$/ZnS Heterojunction to Achieve Outstanding Oxygen Evolution Performance, Angew. Chem. Int. Ed. 60 (2021) 19435–19441, https://doi.org/10.1002/anie.202107731.
[34] Z. Wang, X. Liao, M. Zhou, F. Huang, K.A. Owusu, J. Li, Z. Lin, Q. Sun, X. Hong, C. Sun, Y.-B. Cheng, Y. Zhao, L. Mai, Interfacial and Vacancies Engineering of Copper Nickel Sulfide for Enhanced Oxygen Reduction and Alcohols Oxidation Activity, Energy Environ. Mater. (2022) 1–11, https://doi.org/10.1002/eem2.12409.
[35] Z. Zhao, S. Li, C. Li, Z. Liu, D. Li, Hollow CoS_2@C nanocubes for high-performance sodium storage, Appl. Surf. Sci. 519 (2020), 146268, https://doi.org/10.1016/j.apsusc.2020.146268.
[36] L. Wen, J. Yu, C. Xing, D. Liu, X. Lyu, W. Cai, X. Li, Flexible vanadium-doped Ni_2P nanosheet arrays grown on carbon cloth for an efficient hydrogen evolution reaction, Nanoscale 11 (2019) 4198–4203, https://doi.org/10.1039/C8NR10167A.
[37] Y. Zhang, J. Shi, Z. Huang, X. Guan, S. Zong, C. Cheng, B. Zheng, L. Guo, Synchronous construction of CoS_2 in-situ loading and S doping for g-C_3N_4: Enhanced photocatalytic H_2-evolution activity and mechanism insight, Chem. Eng. J. 401 (2020), 126135, https://doi.org/10.1016/j.cej.2020.126135.
[38] L. Sun, M. Gao, Z. Jing, Z. Cheng, D. Zheng, H. Xu, Q. Zhou, J. Lin, 1 T-Phase Enriched P doped WS_2 nanosphere for highly efficient electrochemical hydrogen evolution reaction, Chem. Eng. J. 429 (2022), 132187, https://doi.org/10.1016/j.cej.2021.132187.
[39] H. Rachna Devi, O. Yadorao Bisen, Z. Chen, K. Kar Nanda, Spatially dispersed one-dimensional carbon architecture on oxide framework for oxygen electrochemistry, Chem. Eng. J. 433 (2021), 133649, https://doi.org/10.1016/j.cej.2021.133649.
[40] G. Zhou, X. Wu, M. Zhao, H. Pang, L. Xu, J. Yang, Y. Tang, Interfacial Engineering-Triggered Bifunctionality of CoS_2/MoS_2 Nanocubes/Nanosheet Arrays for High-Efficiency Overall Water Splitting, ChemSusChem 14 (2021) 699–708, https://doi.org/10.1002/cssc.202002338.
[41] W. Yuan, T. Jiang, X. Fang, Y. Fan, S. Qian, Y. Gao, N. Cheng, H. Xue, J. Tian, Interface engineering of S-doped Co_2P@Ni_2P core–shell heterostructures for efficient and energy-saving water splitting, Chem. Eng. J. 439 (2022), 135743, https://doi.org/10.1016/j.cej.2022.135743.
[42] J. Dai, Y. Zhu, Y. Chen, X. Wen, M. Long, X. Wu, Z. Hu, D. Guan, X. Wang, C. Zhou, Q. Lin, Y. Sun, S.C. Weng, H. Wang, W. Zhou, Z. Shao, Hydrogen spillover in complex oxide multifunctional sites improves acidic hydrogen evolution electrocatalysis, Nat. Commun. 13 (2022) 1189, https://doi.org/10.1038/s41467-022-28843-2.
[43] G. Song, S. Luo, Q. Zhou, J. Zou, Y. Lin, L. Wang, G. Li, A. Meng, Z. Li, Doping and heterojunction strategies for constructing V-doped Ni_3FeN/Ni anchored on N-doped graphene tubes as an efficient overall water splitting electrocatalyst, J. Mater. Chem. A 10 (2022) 18877–18888, https://doi.org/10.1039/D2TA03143D.
[44] J. Song, Y. Chen, H. Huang, J. Wang, S.-C. Huang, Y.-F. Liao, A.E. Fetohi, F. Hu, H.-Y. Chen, L. Li, X. Han, K.M. El-Khatib, S. Peng, Heterointerface Engineering of Hierarchically Assembling Layered Double Hydroxides on Cobalt Selenide as Efficient Trifunctional Electrocatalysts for Water Splitting and Zinc-Air Battery, Adv. Sci. 9 (2022) 2104522, https://doi.org/10.1002/advs.202104522.
[45] T. Xiao, Y. Yang, M. Yang, W. Liu, M. Li, M. Ren, F. Cai, Y. Wang, CoOOH-hierarchical porous carbon-sulfur as an excellent cathode for Li-S batteries, J. Alloy. Compd. 923 (2022), 166334, https://doi.org/10.1016/j.jallcom.2022.166334.
[46] Q. Zhang, W. Xiao, W.H. Guo, Y.X. Yang, J.L. Lei, H.Q. Luo, N.B. Li, Macroporous Array Induced Multiscale Modulation at the Surface/Interface of $Co(OH)_2$/NiMo Self-Supporting Electrode for Effective Overall Water Splitting, Adv. Funct. Mater. 31 (2021) 2102117, https://doi.org/10.1002/adfm.202102117.
[47] S. Ji, T. Li, Z. Gao, Y.-Y. Song, J.-J. Xu, Boosting the Oxygen Evolution Reaction Performance of CoS_2 Microspheres by Subtle Ionic Liquid Modification, Chem. Commun. 54 (2018) 8765–8768, https://doi.org/10.1039/C8CC05352A.
[48] Q. Li, Q. Jiao, Y. Yan, H. Li, W. Zhou, T. Gu, X. Shen, C. Lu, Y. Zhao, Y. Zhang, H. Li, C. Feng, Optimized Co–S bonds energy and confinement effect of hollow MXene@CoS_2/NC for enhanced sodium storage kinetics and stability, Chem. Eng. J. 450 (2022), 137922, https://doi.org/10.1016/j.cej.2022.137922.
[49] M. Chen, D. Liu, J. Feng, P. Zhou, L. Qiao, W. Feng, Y. Chen, K. Wei Ng, S. Wang, W. Fai Ip, H. Pan, In-situ generation of Ni-CoOOH through deep reconstruction for durable alkaline water electrolysis, Chem. Eng. J. 443 (2022) 136432, https://doi.org/10.1016/j.cej.2022.136432.
[50] L. Xia, L. Bo, W. Shi, Y. Zhang, Y. Shen, X. Ji, X. Guan, Y. Wang, J. Tong, Defect and interface engineering of templated synthesis of hollow porous Co_3O_4/$CoMoO_4$ with highly enhanced electrocatalytic activity for oxygen evolution reaction, Chem. Eng. J. 452 (2023), 139250, https://doi.org/10.1016/j.cej.2022.139250.
[51] J. Hong, M. Chen, L. Zhang, L. Qin, J. Hu, X. Huang, C. Zhou, Y. Zhou, T. Wågberg, G. Hu, Asymmetrically Coupled Co Single-atom and Co Nanoparticle in Double-shelled Carbon-based Nanoreactor for Enhanced Reversible Oxygen Catalysis, Chem. Eng. J. 455 (2022), 140401, https://doi.org/10.1016/j.cej.2022.140401.
[52] Y. Liu, X. Liu, A.R. Jadhav, T. Yang, Y. Hwang, H. Wang, L. Wang, Y. Luo, A. Kumar, J. Lee, H.T.D. Bui, M.G. Kim, H. Lee, Unraveling the Function of Metal-Amorphous Support Interactions in Single-Atom Electrocatalytic Hydrogen Evolution, Angew. Chem. Int. Ed. 61 (2022) e202114160.
[53] Z. Luo, Q. Peng, Z. Huang, L. Wang, Y. Yang, J. Dong, T.T. Isimjan, X. Yang, Fine-tune d-band center of cobalt vanadium oxide nanosheets by N-doping as a robust overall water splitting electrocatalyst, J. Colloid Interface Sci. 629 (2023) 111–120, https://doi.org/10.1016/j.jcis.2022.09.069.